REGULAR PAPER

Ni/Au contacts to corundum α-Ga$_2$O$_3$

Fabien C.-P. Massabuau[1*] [iD], Francesca Adams[2], David Nicol[1] [iD], John C. Jarman[2] [iD], Martin Frentrup[2], Joseph W. Roberts[3], Thomas J. O'Hanlon[4] [iD], Andras Kovács[5], Paul R. Chalker[3] [iD], and R. A. Oliver[2] [iD]

[1]Department of Physics, University of Strathclyde, Glasgow G4 0NG, United Kingdom
[2]Department of Material Science and Metallurgy, University of Cambridge, Cambridge CB3 0FS, United Kingdom
[3]School of Engineering, University of Liverpool, Liverpool L69 3GH, United Kingdom
[4]Plymouth Electron Microscopy Centre, University of Plymouth, Plymouth PL4 8AA, United Kingdom
[5]Ernst Ruska-Centre for Microscopy and Spectroscopy with Electrons, Forschungszentrum Jülich, D-52425 Jülich, Germany

*E-mail: f.massabuau@strath.ac.uk

The structural, chemical and electrical properties of Ni/Au contacts to the atomic layer deposited α-Ga$_2$O$_3$ were investigated. Ni forms a Schottky contact with α-Ga$_2$O$_3$, irrespectively of the post-annealing temperature. No sign of metal oxidation was observed at the metal-semiconductor interface (unlike what is observed for other metals like Ti), and instead, the metallurgical processes of the Ni–Au bilayer dominate the electrical properties. It is found that 400 °C–450 °C is the optimal annealing temperature, which allows for metal diffusion to heal gaps at the metal/semiconductor interface, but is not sufficient for Ni and Au to significantly interdiffuse and form an alloy with compositional inhomogeneities. © 2023 The Author(s). Published on behalf of The Japan Society of Applied Physics by IOP Publishing Ltd

1. Introduction

Over the last decade, gallium oxide (Ga$_2$O$_3$) has emerged as a promising candidate for future wide bandgap optoelectronics, with applications entailing high-power electronics and solar-blind sensing.[1–3] Ga$_2$O$_3$ is a highly polymorphic compound, with reported crystallographic phases labelled α, β, κ, γ and δ.[4–6] The β-phase is the thermodynamically stable phase and has therefore received the most attention so far. In comparison, α-Ga$_2$O$_3$ is metastable but worthy of interest due to its wider bandgap and potential for bandgap engineering through alloying with other semiconducting sesquioxides.[7–9] A consequence of that metastability is that progress with material synthesis has developed slower than for the β-phase, but nowadays strategies have been designed to reliably produce the metastable phases using most conventional deposition methods.[10,11]

Metal contacts are a central component of semiconductor devices, and the development of new semiconductor materials goes hand in hand with the development of the metal contacts that allow the new device to fulfil its purpose. For example, in the context of photodetectors, ohmic contacts often result in greater responsivity but slower response time, while Schottky contacts are associated with faster response time and lower dark current.[12,13] Being the most studied polymorph, metal contacts to β-Ga$_2$O$_3$ have been investigated by several groups.[14–18] These studies demonstrated that the conventional description of metal-semiconductor contacts borrowed from the Schottky–Mott model—which states that the rectifying or ohmic nature of the contact is determined by the work-function of the metal and the electron affinity of the semiconductor—falls short with Ga$_2$O$_3$ where many other factors have been found to play a non-negligible role. These include interfacial reaction between the oxide semiconductor and the metal,[19–21] semiconductor orientation,[18] morphology and thermal treatment.[17] In comparison, metal contacts to the metastable phases have been overlooked, and the behaviour of contacts in these phases are often assumed to be identical to their β-phase equivalent. A phase-specific study of contacts is however, necessary since many of the aforementioned factors—electron affinity, crystal orientation, chemical stability and morphology—are indeed, phase-dependent.

In a previous report, we investigated Ti/Au as a metal candidate for ohmic contact to α-Ga$_2$O$_3$ and highlighted that the electrical performance of the contact was the result of the competition between different processes including Ti oxidation by α-Ga$_2$O$_3$ with a mosaic structure, Ti-Au interdiffusion, and Au crystallization.[22] The different rates of each of these processes led to strong variations in contact performance with post-deposition treatment.

In the present study, we turn our attention to Ni/Au as a candidate Schottky contact to α-Ga$_2$O$_3$. In β-Ga$_2$O$_3$, Ni has been shown to form Schottky contacts[13,15,18,23,24] but the Fermi level pinning and Schottky barrier height was shown to strongly depend on the crystal orientation,[15,18,23] metal deposition method and thermal treatment.[24] Already in β-Ga$_2$O$_3$, little attention was paid to the other metallurgical and chemical mechanisms that arise in the metal contact stack. As Ni contacts are often coated with Au, the interaction between these two materials needs to be considered. Indeed, previous studies on GaN have demonstrated that great amounts of diffusion between Ni and Au occurred at low annealing temperatures,[25–27] and even leading to dewetting at greater temperatures.[28] In the present study we look into the properties of Ni/Au contacts to α-Ga$_2$O$_3$, and highlight the interplay between metallurgical, chemical and electrical processes occurring within them.

2. Experimental methods

Films of non-intentionally n-doped α-Ga$_2$O$_3$ with thickness of ca. 250 nm were grown on c-plane sapphire (α-Al$_2$O$_3$) substrates by plasma-enhanced atomic layer deposition (PEALD) using an Oxford Instruments OpAL reactor at a temperature of 250 °C—a full description of the growth process can be found in Ref. 29. From previous investigations,[29,30] it is known that

under these growth conditions, the resulting α-Ga$_2$O$_3$ films grow epitaxially on the α-Al$_2$O$_3$ substrate with [0001]$_{Ga2O3}$ || [0001]$_{Al2O3}$ and [11$\bar{2}$0]$_{Ga2O3}$ || [11$\bar{2}$0]$_{Al2O3}$. The films consist dominantly of α-Ga$_2$O$_3$ columns, with amorphous and κ-Ga$_2$O$_3$ inclusions located between the columns.[30] The films were unintentionally n-doped, as was observed using X-ray absorption spectroscopy and soft X-ray photoelectron spectroscopy by Swallow et al. on comparable α-Ga$_2$O$_3$ films deposited by PEALD.[31]

Following cleaning in acetone and isopropyl alcohol, metal contacts were defined using ultraviolet lithography and thermal evaporation. Shipley s1813 positive photoresist was developed with MF-319, an aqueous developer containing dilute tetramethylammonium hydroxide (TMAH), after a short post-exposure treatment with chlorobenzene to produce the undercut profile required for the metal lift-off process. After resist processing, 20 nm Ni and 80 nm Au were evaporated by resistive thermal evaporation from tungsten boats, and the patterns were lifted off in acetone. The contact structure consisted of circular pads 180 μm in diameter and spaced 500 μm apart. The samples were then annealed using rapid thermal annealing for 2 min in N$_2$ ambient at temperatures ranging from 350 °C to 600 °C, while one sample was kept unannealed.

Atomic force microscopy (AFM) using a Bruker Dimension Icon Pro microscope operating in peak force tapping mode was employed to record the topography of the α-Ga$_2$O$_3$ surface before and after annealing.

X-ray diffraction (XRD) using a Philips X'pert MRD diffractometer consisting of a Cu K$_{\alpha1}$ source, a four-bounce Ge crystal monochromator, and a three-bounce Ge crystal analyser was employed to record the structure of the samples before and after annealing.

Photoelectric characterisation was performed using Keithley 6487 source-meter unit coupled to a Signatone probe station. A Thorlabs SL S204 Deuterium light source coupled to a SolarLS ML44 monochromator was used to excite the sample with a 240 nm light beam.

To observe the atomic and chemical structure of the samples, lamellae were prepared by focussed ion beam sputtering, and high-angle annular dark-field scanning transmission electron microscopy (HAADF-STEM) imaging and energy-dispersive X-ray spectroscopy (EDX) measurements were conducted using an aberration-corrected FEI Titan microscope[32] operated at 200 kV and with ADF detector semi-angle of 69 mrad. EDX compositional maps were obtained using the Cliff–Lorimer factor method.[33]

3. Results and discussion

Figure 1(a) shows XRD 2θ-ω scans for the as-deposited and annealed samples. Each diffractogram exhibits an intense sharp peak at 41.7° corresponding to the 0006 reflection of the α-Al$_2$O$_3$ substrate as well as a peak near 40.1°–40.2° associated with the 0006 reflection of the α-Ga$_2$O$_3$ film. Slight variations in α-Ga$_2$O$_3$ peak position are visible upon annealing, in agreement with previous reports that annealing induces strain relaxation.[22,34] Reflections associated with the metal contact can also be observed. In the as-deposited structure, the 111 reflection of Au can be seen at 38.2°, while the 111 reflection of Ni at 44.8° is barely visible, which is not unexpected given the thinness and potential low-crystallinity of the evaporated Ni layer.
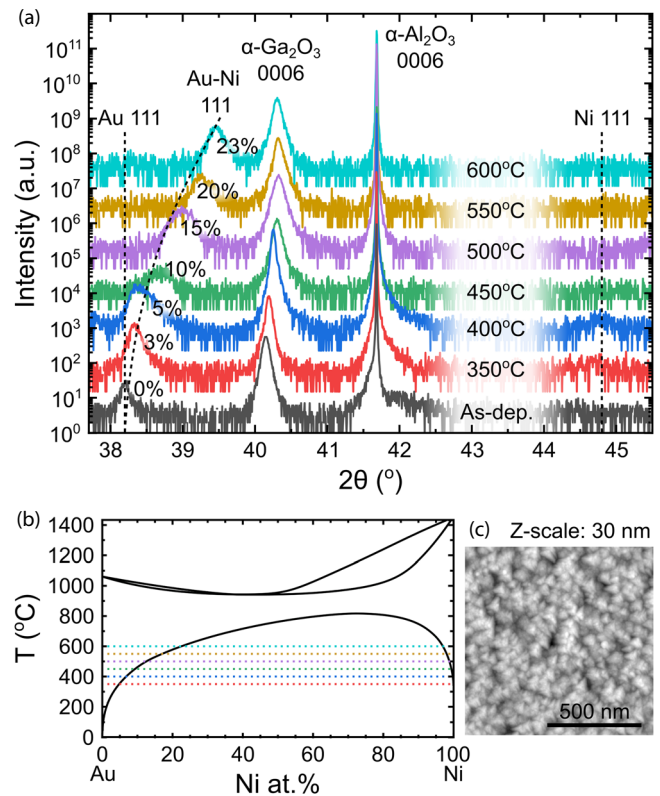

Fig. 1. (Color online) (a) Symmetric 2θ-ω XRD scans of the samples annealed at different temperatures. (b) Redrawn phase diagram for Au–Ni. (c) AFM topography image of the α-Ga$_2$O$_3$ surface.

For the structures that were annealed, we can see that the Au 111 peak (in the as-deposited sample) shifts substantially towards greater angles upon annealing at higher temperatures. This could be indicative of the formation of an Au–Ni alloy from the initial Ni–Au metal bilayer. Using the peak position to infer the lattice plane spacing and alloy composition assuming Vegard's law applies[35] we find that Au–Ni interdiffusion is limited at low annealing temperatures, with the Au–Ni alloy annealed at 400 °C containing only 5% of Ni, but increases significantly for greater temperatures, reaching 23% of Ni for the Au–Ni alloy annealed at 600 °C—see compositions labelled in Fig. 1(a). Looking at the phase diagram for Au–Ni [Fig. 1(b)], we can see that the alloy compositions obtained from XRD follow the expected miscibility of Ni in Au. It is perhaps surprising that a 2 min anneal is sufficient to reach an alloy composition close to that expected at thermodynamic equilibrium. We note that our results are aligned with previous reports from Herz et al. who studied a greater range of anneal conditions on Ni–Au bilayers and observed that this interdiffusion marked the early stages of the dewetting process.[28]

AFM was conducted to verify that the α-Ga$_2$O$_3$ was not significantly affected by the annealing treatment. Indeed, we report no significant changes in topography, with the RMS roughness remaining within the 3.8–4.8 nm range across the whole sample set—in agreement with our previous observations.[22] Figure 1(c) shows a typical AFM scan of the α-Ga$_2$O$_3$ surface, dominated by triangular features representative of the symmetry of the α crystal phase.

The electrical behaviour of the contacts was measured. Since the films were nominally undoped and hence too
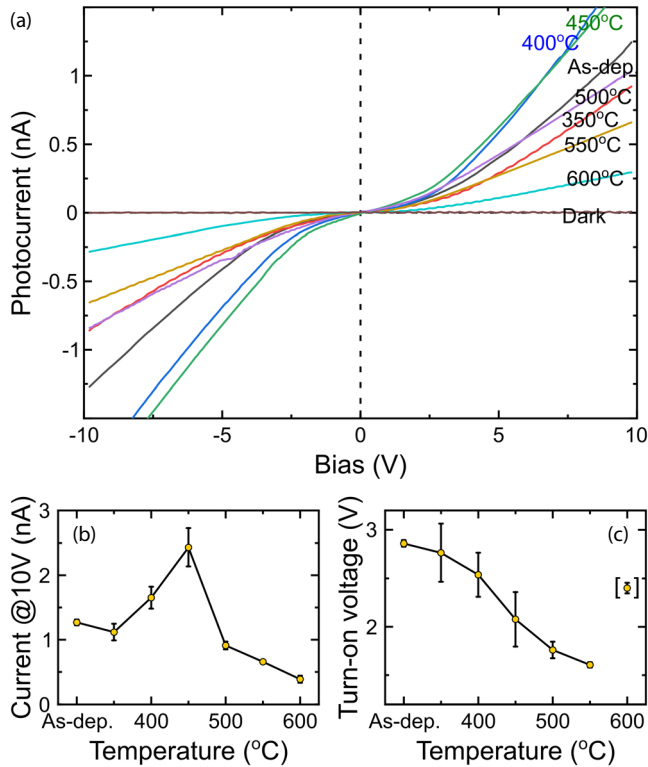
Fig. 2. (Color online) (a) Photo *I–V* characteristics, (b) photocurrent at 10 V, and (c) turn-on voltage of the samples annealed at different temperatures.

resistive, the *I–V* characteristics were obtained under 240 nm light illumination to increase their conductivity. Liu et al. showed that the ohmic or rectifying nature of the contact was not affected by light illumination.[13] Figure 2(a) shows the photocurrent versus voltage curve for all the samples, alongside the typical dark *I–V* characteristic. The dark current is limited by the noise of the system, but we can already clearly see that the samples are acting as solar-blind detectors, as the photocurrent under 240 nm illumination and 10 V bias is 2–3 orders of magnitudes greater than the dark current at the same voltage.

The main observation from Figure 2(a) is that all the *I–V* curves show that Ni/Au forms a rectifying contact to α-Ga$_2$O$_3$, irrespective of the post-deposition annealing conditions. This is in line with previous reports on β-Ga$_2$O$_3$.[13,15,18,23,24] This finding can be partially rationalised by the fact that the electron affinity of (0001)-oriented α-Ga$_2$O$_3$ has been calculated at 3.62 eV,[36] while the

workfunctions of (111)-oriented Ni and Au are 5.24 eV and 5.33 eV, respectively.[37]

Besides the rectifying behaviour common for all the contact structures, we observe variations in photocurrent at 10 V [Fig. 2(b)] and turn-on voltage [Fig. 2(c)]. Figure 2(b) shows that the photocurrent increases about two-fold when the structure is annealed at 400 °C–450 °C, then rapidly decreases if the anneal is conducted at greater temperatures. In terms of turn-on voltage in Fig. 2(c), we observe that the turn-on voltage (note that this is under illumination) is relatively stable at low annealing temperatures, then gradually decreases over the ca. 400 °C–500 °C range, then stabilises again for greater annealing temperatures (note that the datapoint at 600 °C could not be reliably determined due to the noisy signal and shallow increase of the *I–V* curve for this sample).

Collating our observations from Figs. 1(a) and 2(b), 2(c) allow us to distinguish 3 main regimes: (i) A first regime seen when there is no anneal or the annealing temperature is low (⩽350 °C) where the structure is close to as-deposited; (ii) a second regime of medium (400 °C–450 °C) annealing conditions where the Au and Ni just start interdiffusing, the photocurrent is maximal, and the turn-on voltage decreases; and finally (iii) a third regime of harsher annealing conditions (⩾500 °C) where Au–Ni alloying is significantly more pronounced, and where the photocurrent is degraded. From Fig. 2(b), medium annealing conditions are favourable to the electric performance of the contact structure.

Figure 3 presents HAADF-STEM images and elemental maps extracted from EDX measurements of samples corresponding to the 3 regimes highlighted above.

Figure 3(a) shows the contact structure annealed at 350 °C, that is, where the anneal temperature is too low to induce significant changes. The image shows that the sample and contact structure is as expected from the deposition procedure. The α-Ga$_2$O$_3$ film consists of triangular columns of high crystalline quality which thread up to the top surface of the film (as shown by the high resolution image in the inset) with amorphous material between the columns (slightly darker contrast in the film), in line with previous cross-sectional images of PEALD Ga$_2$O$_3$ samples.[22,29,30] In places, we observe a significant gap between α-phase columns, where the top surface of the film lies ca. 60 nm below the rest of the film. This was observed in other films where Ti contacts were deposited,[22] but not on films without contacts.[30,34] In our previous work we noticed that the
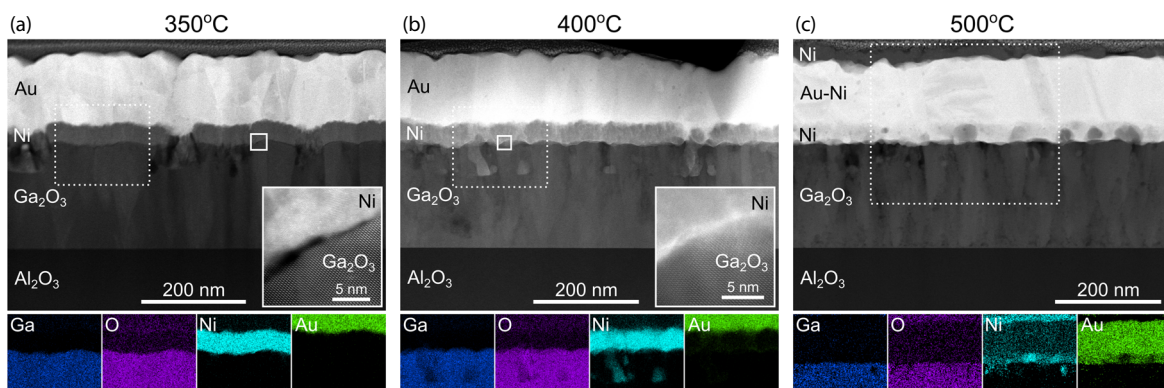

Fig. 3. (Color online) TEM images and EDX maps of the samples annealed at (a) 350 °C, (b) 400 °C, and (c) 500 °C.

developer solution containing tetramethylammonium hydroxide (TMAH) used during contact deposition could etch the film,[34] hence minimal exposure was used. More recent reports have found that TMAH etched amorphous Ga_2O_3,[38] but not β-Ga_2O_3.[39] We therefore attribute these features to the preferential etching of amorphous Ga_2O_3 by the TMAH. Analysis of the Ga_2O_3/Ni interface region, in inset of Fig. 3(a), reveals that the Ni layer is polycrystalline, and while it is directly deposited on top of the α-Ga_2O_3 film, we note the presence of a number of nanometer-thick gaps between the α-Ga_2O_3 and Ni. These gaps certainly originate from the deposition process of Ni on the semiconductor. The Au layer is also polycrystalline, but forms already large grains as could be expected from the Au reflection seen by XRD in Fig. 1(a). Looking at the interface region by EDX, we can see that all the layers are chemically distinct, with no sign of diffusion between the layers.

Figure 3(b) shows the structure annealed at 400 °C, that is, the structure at the onset of which Ni–Au alloy becomes noticeable by XRD, and also the structure that exhibits the best electrical properties alongside that annealed at 450 °C. The structure is very similar to that shown in Fig. 3(a), and the major difference to be noted is that the interface between the crystalline α-Ga_2O_3 and Ni films no longer contains gaps (see inset). We also observe that the Ni film starts appearing more granular, and EDX analysis shows that Au is present at the Ni grain boundaries. We note that the α-Ga_2O_3/Ni interface looks rougher, which is difficult to interpret with certainty. This is probably due to a projection effect in TEM as the columns are of similar dimensions as the thickness of the TEM lamella. The faint presence of Au at the interface, however, makes it difficult to draw conclusive interpretations of the contrast at the interface. We rule out surface reconstruction effects at this temperature, as our AFM data show no difference in topography upon annealing. Lastly, in the troughs formed by selective etching of amorphous Ga_2O_3 by TMAH, Ni is still present in its metallic form—probably formed by the wetting of the Ni that was initially sputtered inside these throughs. It appears more encapsulated within the Ga_2O_3 matrix; however, we cannot draw firm conclusions as these Ni inclusions are of small dimensions and this could be a projection effect from the TEM. This image overall shows that this annealing condition is the onset of metal atoms diffusion, which main effect here is to "heal" the gaps at the interface with the Ga_2O_3 and likely the reason for the improved electrical performances.

Figure 3(c) presents the cross-sectional analysis of the sample annealed at 500 °C, that is, the regime where XRD detected significant mixing between Au and Ni, and the photocurrent was significantly lower. As in Figs. 3(a) and 3(b), we observed the presence of Ni in the troughs formed by selective etching of amorphous Ga_2O_3 by TMAH. As above, these Ni-containing precipitates (their exact chemical nature cannot be conclusively ascertained due to projection effects in the TEM) probably originate from the initial sputtering of Ni inside the troughs. The most noticeable feature in this image is the significant interdiffusion between Au and Ni. The Ni/Au structure can now be described as a 3-layer structure. Starting from the bottom, what used to be a uniform Ni layer is now a layer containing roughly spherical Ni-rich precipitates (ca. 91% Ni) within a Au–Ni solid

solution (ca. 46% Ni). Above that layer, we find a Au–Ni alloy layer of slightly lower Ni fraction (ca. 17% Ni). Finally, a top-most layer of NiO_x has formed. Outdiffusion of Ni to the surface of Ni/Au contacts have also been reported in literature for GaN contacts annealed at similar temperatures in oxidising atmospheres.[26,27] Here, since the anneal was conducted under N_2 ambient, we estimate that the top-most NiO_x layer oxidised when the sample was exposed to air after the anneal. In this structure, the Ga_2O_3 film is therefore in contact with a Ni–Au alloy layer with a very variable Ni fraction, resulting in highly non-uniform Schottky barrier heights across the contact area.

An interesting observation to be made is that—in comparison to Ti contacts to α- and β-Ga_2O_3 annealed at the same temperatures[19,22]—no redox reaction has occurred between the semiconductors and the metal, which concurs with findings for Ni on β-Ga_2O_3.[20] This is not surprising as the Gibbs free energy for the Ni/NiO couple is greater than that of Ga/(β-)Ga_2O_3 at all temperatures and partial pressures of O_2, meaning that oxidation of the Ni metal contact by Ga_2O_3 is not expected at any annealing temperature.

4. Conclusions

We have investigated the structural, chemical and electrical properties of Ni contacts to α-Ga_2O_3 and linked the electrical performance to the chemical and metallurgical processes at play during metal contact thermal treatment. Ni forms a Schottky contact with α-Ga_2O_3, irrespectively of the post-annealing temperature. No sign of metal oxidation was observed at the metal-semiconductor interface (unlike with other metals like Ti). Instead, we find that the metallurgical processes of the Ni–Au bilayer dominate the impact on the electrical properties. For low ($T \leqslant 350$ °C) temperature anneal, the contact is negatively affected by small gaps present at the metal/semiconductor interface stemming from the metal deposition. For medium (400 °C $\leqslant T \leqslant$ 450 °C) anneal, metal diffusion starts becoming thermally activated, allowing to heal the interface gaps, but is not sufficient for significant Au–Ni interdiffusion to occur. For greater ($T \leqslant$ 500 °C) anneals, the increase in metal diffusion provokes significant Au–Ni interdiffusion leading to highly non-uniform interface properties across the contact area.

ORCID iDs

Fabien C.-P. Massabuau https://orcid.org/0000-0003-1008-1652
David Nicol https://orcid.org/0000-0003-3746-5138
John C. Jarman https://orcid.org/0000-0001-8095-8603
Thomas J. O'Hanlon https://orcid.org/0000-0002-4700-7141

Paul R. Chalker https://orcid.org/0000-0002-2295-6332
R. A. Oliver https://orcid.org/0000-0003-0029-3993

1) S. J. Pearton, J. Yang, P. Cary, F. Ren, J. Kim, M. Tadjer, and M. Mastro, Appl. Phys. Rev. **5**, 011301 (2018).
2) D. Kaur and M. Kumar, Adv. Opt. Mater. **9**, 2002160 (2021).
3) A. Green et al., APL Mater. **10**, 029201 (2022).
4) R. Roy, V. Hill, and E. Osborn, J. Am. Chem. Soc. **74**, 719 (1952).
5) H. Playford, A. Hannon, E. Barney, and R. Walton, Chem.—Eur. J. **19**, 2803 (2013).
6) I. Cora, F. Mezzadri, F. Boschi, M. Bosi, M. Caplovicova, G. Calestani, I. Dodony, B. Pecz, and R. Fornari, CryslEngComm **19**, 1509 (2017).
7) S. Fujita and K. Kaneko, J. Cryst. Growth **401**, 588 (2014).
8) J. Jinno et al., Sci. Adv. **7**, eabd5891 (2021).
9) A. Barthel, J. Roberts, M. Napari, M. Frentrup, T. Huq, A. Kovacs, R. Oliver, P. Chalker, T. Sajavaara, and F. Massabuau, Micromachines **11**, 1128 (2020).
10) K. Kaneko, K. Uno, R. Jinno, and S. Fujita, J. Appl. Phys. **131**, 090902 (2022).
11) D. Yang, B. Kim, T. Eom, Y. Park, and H. Jang, Elec. Mater. Lett. **18**, 113 (2022).
12) C. Xie, X. T. Lu, X. W. Tong, Z. X. Zhang, F. X. Liang, L. Liang, L. B. Luo, and Y. C. Wu, Adv. Func. Mater. **29**, 1806006 (2019).
13) Z. Liu et al., J. Phys. D: Appl. Phys. **53**, 085105 (2020).
14) H. Kim, SN Appl. Sci. **4**, 27 (2022).
15) L. Porter and J. Hajzus, J. Vac. Sci. Tech. A **38**, 031005 (2020).
16) M. H. Lee and R. Peterson, J. Mater. Res. **36**, 4771 (2021).
17) Y. Yao, R. Davis, and L. Porter, J. Elec. Mater. **46**, 2053 (2017).
18) L. Lyle, K. Jiang, E. Favela, K. Das, A. Popp, Z. Galazka, G. Wagner, and L. Porter, J. Vac. Sci. Tech. A **39**, 033202 (2021).
19) M. H. Lee and R. Peterson, APL Mater. **7**, 022524 (2019).
20) H. Aller, X. Yu, A. Wise, R. Howell, A. McGaughey, and J. Malen, Nano Lett. **19**, 8533 (2019).
21) L. Lyle, T. Back, C. Bowers, A. Green, K. Chabak, D. Dorsey, E. Heller, and L. Porter, APL Mater. **9**, 061104 (2021).
22) F. Massabuau, D. Nicol, F. Adams, J. Jarman, J. Roberts, A. Kovacs, P. Chalker, and R. Oliver, J. Phys. D: Appl. Phys. **54**, 384001 (2021).
23) E. Farzana, Z. Zhang, P. Paul, A. Arehart, and S. Ringe, Appl. Phys. Lett. **110**, 202102 (2017).
24) H. Kim, S. Kyoung, T. Kang, J. Y. Kwon, K. Kim, and Y. Rim, J. Mater. Chem. C **7**, 10953 (2019).
25) J. Sheu, Y. Su, G. Chi, W. Chen, C. Chen, J. Hong, Y. Yu, C. Wang, and E. Lin, J. Appl. Phys. **83**, 3172 (1998).
26) J. Smalc-Koziorowska, S. Grzanka, E. Litwin-Staszewska, R. Piotrzkowski, G. Nowak, M. Leszczynski, P. Perlin, E. Talik, J. Kozubowski, and S. Krukowski, Solid-State Elec. **54**, 701 (2010).
27) L. C. Chen, F. R. Chen, J. J. Kai, L. Chang, J. K. Ho, C. S. Jong, C. Chiu, C. N. Huang, C. Y. Chan, and K. K. Shih, J. Appl. Phys. **86**, 3826 (1999).
28) A. Herz, D. Wang, T. Kups, and P. Schaaf, J. Appl. Phys. **116**, 044307 (2014).
29) F. C.-P. Massabuau et al., Proc. SPIE **11687**, 116870Q (2021).
30) J. Roberts, J. Jarman, D. Johnstone, P. Midgley, P. Chalker, R. Oliver, and F. C.-P. Massabuau, J. Cryst. Growth **487**, 23 (2018).
31) J. Swallow et al., Chem. Mater. **32**, 8460 (2020).
32) A. Kovacs, R. Schierholz, and K. Tillmann, J. Large-Scale Res. Facilities **2**, A43 (2016).
33) G. Cliff and G. Lorimer, J. Micro. **103**, 203 (1975).
34) J. Moloney et al., J. Phys. D: Appl. Phys. **52**, 475101 (2019).
35) A. Crawley and D. Fabian, J. Institute Met. **94**, 39 (1966).
36) Y. Hinuma, T. Gake, and F. Oba, Phys. Rev. Mat. **3**, 084605 (2019).
37) G. Derry, M. Kern, and E. Worth, J. Vac. Sci. Tech. A **33**, 060801 (2015).
38) Z. Han, H. Liang, W. Huo, X. Zhu, X. Du, and Z. Mei, Adv. Opt. Mater. **8**, 1901833 (2020).
39) H. Okumura and T. Tanaka, Jpn. J. Appl. Phys. **58**, 120902 (2019).